GSA Data Repository 2018048

Earth's oldest mantle peridotites show full record of late accretion

J. van de Löcht[1*], J.E. Hoffmann[2], C. Li[2], Z. Wang[2], H. Becker[2], M.T. Rosing[3], R. Kleinschrodt[1], C. Münker[1]

[1)] Universität zu Köln, Institut für Geologie und Mineralogie, Zülpicher Str. 49b, Köln, Germany

[2)] Freie Universität Berlin, Institut für Geologische Wissenschaften, Malteserstr. 74-100, 12249 Berlin, Germany

[3)] China University of Geosciences, No 388 Lumo Road, 430074, Wuhan, China

[4)] NordCEE, Copenhagen University, Øster Voldgade 3-5, 1350 København., Denmark

** corresponding author: loechtj@uni-koeln.de*

SUPLEMENTARY METHODS

Sample preparation

Samples of about 2-4 kg were cleaned for visible alteration domains using a diamond saw, sanded and washed and crushed to up to 0.5 cm chips using a stainless steel jaw crusher. About 500-1000 g fine sample powder of each sample was produced from rock chips using an agate ball mill.

In order to evaluate potential metal contamination due to the use of the stainless steel jaw crusher, aliquots of three samples (12B ~100g, 10-20C ~30g and 10-31 ~80g) and a piece of the stainless steel were processed in a different way. Rock pieces were sanded by corundum and crushed by hand in plastic bags avoiding any contact with metal tools. The samples were than powdered using an agate ball mill and/or agate mortar.

Major element analysis

Whole rock chemistry using X-ray fluorescence

Major element contents were determined on $Li_2B_4O_7$-flux fusion discs by X-ray fluorescence using a Philips PW 2400 X-ray spectrometer at Cologne. Analytical uncertainty was estimated to ±1 wt% (2σ) for the major elements based on replicate measurements of in-house reference materials.

Mineral chemistry using electron microprobe

Electron microprobe analyses of polished thin sections were performed on a JEOL JXA-8900RL Superprobe at Cologne. Operating conditions were 20 kV accelerating voltage and 20 nA beam current, using a focussed electron beam. A counting time of 20s on peak and 10s on background was chosen for all elements. A set of natural silicate (for Si, Mg, Ca, Na, K, Mn, Fe) and oxide (for Al, Cr, Ti, Ni) standards was used for calibration and the ZAF-algorithm was used for correction.

Highly siderophile element (HSE) analyses

Sample digestion

About 2.5 g sample powder aliquots were mixed with ^{185}Re-^{190}Os and ^{191}Ir-^{99}Ru-^{194}Pt-^{105}Pd tracer solutions and with reverse aqua regia (2.5 ml 9 M HCl + 5 ml 14 M HNO_3) in a quartz vessel for digestion in a high-pressure asher (HPAS, Anton Parr^{TM}) (Fischer-Gödde et al., 2011). The HPAS vessels were heated to 320 ℃ for about 12 hours at 100 bars.

Os separation and measurement

The Os separation procedure followed the protocol outlined in Fischer-Gödde et al. (2011). The digested sample solutions were transferred into 50 ml centrifuge tubes, and mixed with 2-3 ml chloroform ($CHCl_3$). The mixture was first homogenized by shaking and then centrifuged for 5 minutes in order to extract Os into the $CHCl_3$. The Os-bearing $CHCl_3$ was

transferred into 15 ml PFA beakers with 4 ml distilled HBr. This Os extraction procedure was repeated three times to yield high recovery. The extracted Os-bearing HBr-$CHCl_3$ mixture was heated in closed PFA beakers at 85℃ for 4 hours in order to back-extract Os into the HBr. The chloroform was removed and the Os-bearing HBr was evaporated to dryness. Osmium was further purified by micro-distillation using a H_2SO_4-dichromate solution and trapped into HBr (Cohen and Waters, 1996). After the micro-distillation, the sample was dried down and dissolved into 2 µl HBr. About half of the solution was loaded on platinum filaments and covered with $Ba(OH)_2$ as activator.

Osmium isotope compositions were determined as oxide using a thermal ionization mass spectrometer in negative mode (N-TIMS, Thermal-Finnigan^{TM} Triton) at Freie Universität Berlin. Except of one sample (10-29A) that was measured using Faraday detectors, all other samples were measured using a secondary electron multiplier (SEM). Measured ratios were corrected for isobaric OsO_3- interferences, and mass fractionation was corrected for by using $^{192}Os/^{188}Os = 3.0827$. Measurements of the University of Maryland Os standard solution using SEM yielded for the first measurements (2015) $^{187}Os/^{188}Os = 0.1141 \pm 0.0002$ (2 SD, n=8), measurements (2017) $^{187}Os/^{188}Os = 0.1139 \pm 0.0002$ (2 SD, n=8), and using Faraday detectors $^{187}Os/^{188}Os = 0.11377 \pm 0.00003$ (n=1). Measured $^{187}Os/^{188}Os$ isotope compositions of the samples were corrected for the slight offset from the value of $^{187}Os/^{188}Os = 0.11379 \pm 0.00002$ (Shirey and Walker, 1998) (Table DR3 and Table DR4).

Separation and measurement of other highly siderophile elements

Following the extraction of Os, about 2-2.5 ml aliquots of the aqua regia digestion solution were centrifuged and transferred into 15 ml PFA beakers and evaporated to near dryness. The sample was then converted to chloride form by adding 2-3 ml 9 M HCl twice and 1 ml 1.25 M HCl and drying down.

The chemical separation of Re, Ir, Ru, Pt, Rh and Pd from the matrix followed the procedure reported by Fischer-Gödde et al. (2011) using cation exchange chromatography. The samples were dissolved in 10 ml 0.5 M HCl + 40% acetone solution and loaded onto 10 ml cation exchange resin (Eichrom™ 50W-X8) and the elements of interest were collected into 14 ml HCl-acetone solution, after eluting the matrix.

The collected element cuts were separated into two equal aliquots, one for Re-Ir-Pt measurement and the other for Ru-Pd-Ir-Pt. After evaporating the acetone, the Re-Ir-Pt aliquots were measured by sector-field inductively coupled plasma mass spectrometry (SF-ICPMS, ThermoElectron Element XR) at Freie Universität Berlin, using a Scott-type spray chamber following the methods outlined in Fischer-Gödde et al. (2011). The Ru-Pd-Ir-Pt aliquots were dried down and re-dissolved into 0.5 ml 0.2M HCl. Subsequently, a clean-up procedure for Pd was applied in order to remove Cd using 2 ml Eichrom 50W-X8 resin. The purified Ru-Pd aliquots were dried down and dissolved into 4 ml 0.28 M HNO_3 and then measured using an Aridus desolvator system (Aridus-I) with CeO^+/Ce^+ of < 0.002.

For the concentration calculation of Ir, Ru, Pt and Pd by isotope dilution, the following isotope ratios were used: $^{191}Ir/^{193}Ir$, $^{99}Ru/^{101}Ru$, $^{194}Pt/^{195}Pt$ and $^{105}Pd/^{106}Pd$. $^{111}Cd/^{106}Pd$ ratios were generally low (< 0.01), making an interference correction of Cd on ^{106}Pd negligible.

Duplicate analyses were conducted for two samples (10-11 and 10-22). The relative deviation of HSE concentrations were on average < 5% for Ir and Ru, and <10% for Pt, Os, Re and Pd (10-22 duplicate). Only Pd (10-11duplicate) displays a higher deviation of 18.4%. Ir and Pt were measured on different aliquots of the same digestion, using the Scott-type spray chamber and the Aridus desolvator system. The relative difference of Ir concentration obtained from both aliquots is 0.14% and 2.2%, and <0.7% for Pt concentration obtained from group 2 peridotites, whereas the relative difference of Pt concentrations obtained from the group 1 peridotites is higher (0.95% – 8.71%) due to much lower Pt abundances and lower intensities during the measurements.

A reference material, harzburgite MUH-1 (Meisel and Horan, 2016) was digested and analyzed twice together with the peridotite samples. Duplicate analyses were in good agreement for Os, Ru, however, for Ir, Pt, Pd and Re large discrepancies of 34% for Ir, 86% for Pt, 20% for Pd and 36% for Re between the duplicate digestions were observed (see Table DR2). The large discrepancy for most HSE contents, particularly Pt is probably due to sample heterogeneities (see the compiled data of Meisel and Horan, 2016). However, MUH-1 duplicates still yielded similar $^{187}Os/^{188}Os$.

Typical procedural blanks were between 0.1 and 6 pg for Os, between 1 and 7 pg for Re, between 0.5 and 20 pg for Ir, <7 pg for Ru, <58 pg for Pt and <83 pg for Pd.

SUPPLEMENTARY TEXT AND FIGURES

Ultramafic rocks in the IGC

In the ICG, ultramafic rocks occur as part of supracrustal belts or separate enclaves tectonically intercalated in ca. 3.8 Ga tonalitic gneisses (Nutman et al., 1996; Friend et al., 2002). The ultramafic enclaves are often embedded together with (garnet)-amphibolite and smaller outcrops of cherts that may represent chemical sediments (Friend and Nutman, 2010). Generally, most of the peridotites are strongly altered, except for low strain zones where extremely well preserved peridotites can be found in the central parts of enclaves that can be up to several hundred meters in diameter. Massive dunitic and harzburgitic rocks can be distinguished from layered, cumulate ultramafic to leuco-gabbroic rocks, chemical sediments and other supracrustal amphibolites (Friend et al. 2002).

Moreover, field observations indicate similarities with obducted sequences of oceanic abyssal peridotites at convergent plate margins, according to resent studies, several ultramafic enclaves (including the studied locations) were formed at convergent plate boundaries, as do supra-subduction zone ophiolites in more recent times (e.g., Friend et al., 2002; Nutman et al. 2007; Polat et al. 2015). Accordingly, the Archean craton of West Greenland grew at

convergent plate margins during Eoarchean to Neoarchean times and the structural characteristics of the terrane boundaries are largely consistent with horizontal tectonics, similar to modern style tectonics (e.g., Nutman et al., 2013). This is in good agreement with recent tectono-metamorphic interpretations for the Archean Greenland and North American part of the North Atlantic Craton (e.g., Friend et al., 2002; Hanmer et al., 2002a, 2002b; Nutman et al., 2009; Næraa et al., 2012; 2015; Dziggel et al., 2014, 2017; Komiya et al., 2015; Polat et al., 2015) as well as geochemical data from mafic rocks of the ISB that show similarities to modern subduction suite related rocks (e.g., Polat et al., 2002, 2003; Polat and Hofmann, 2003; Jenner et al., 2009; Hoffmann et al., 2010, 2011). Major elements and PGE concentration obtained from the investigated peridotites are in the range of abyssal peridotites and other mantle tectonites, and thus, consistent with field observations and tectono-metamorphic models proposed for the ICG in the last 15 years.

A minimum age of about 3.8 Ga for the investigated peridotites was estimated based on field relationships to surrounding ~ 3.8 Ga tonalitic gneisses and crosscutting, magmatic ≥ 3.8 Ga dykes (e.g., Friend et al., 2002; Nutman et al., 2007). This is in good agreement with the predominantly Eoarchean Re-depletion ages (TRD) obtained from group 1 peridotites. Moreover, in the >3.81 Ga Ujargssuit Nunât layered intrusion to the east of the studied SOISB locality, Pt-Os model ages even as old as 4.36 Ga were reported (Coggon et al., 2013), but it is ambiguous if these localities remained undisturbed and if they directly relate to the peridotites studied here.

Petrographic sample descriptions and mineral chemistry of olivine

Samples collected south of the Isua Supracrustal Belt (SOISB)

The peridotite exposures and also a number of representative samples from SOISB were described in detail by Friend et al. (2002) and Bennett et al. (2002) (Fig. DR1a). Together with amphibolites and smaller outcrops of cherts that may represent chemical sediments, the peridotite enclaves are embedded in c. 3.8 Ga tonalitic gneisses (Friend et al. 2002). Hence,

the peridotites were already associated with mafic rocks and ocean floor sediments by c. 3.8 Ga, when the IGC tonalites intruded at mid-crustal levels (Nutman et al. 1996; Friend et al. 2002). Bennett et al. (2002) reported Re-Os isotope data for SOISB obtained from peridotites investigated by Friend et al. (2002). One of those samples is from the same mafic-ultramafic body sampled by type 2 peridotites 10-29 A and B, 10-30 and 10-31 (Fig. DR1) and three samples of Bennett et al. (2002) were collected from smaller enclaves northeast of this locality that are not part of our study.

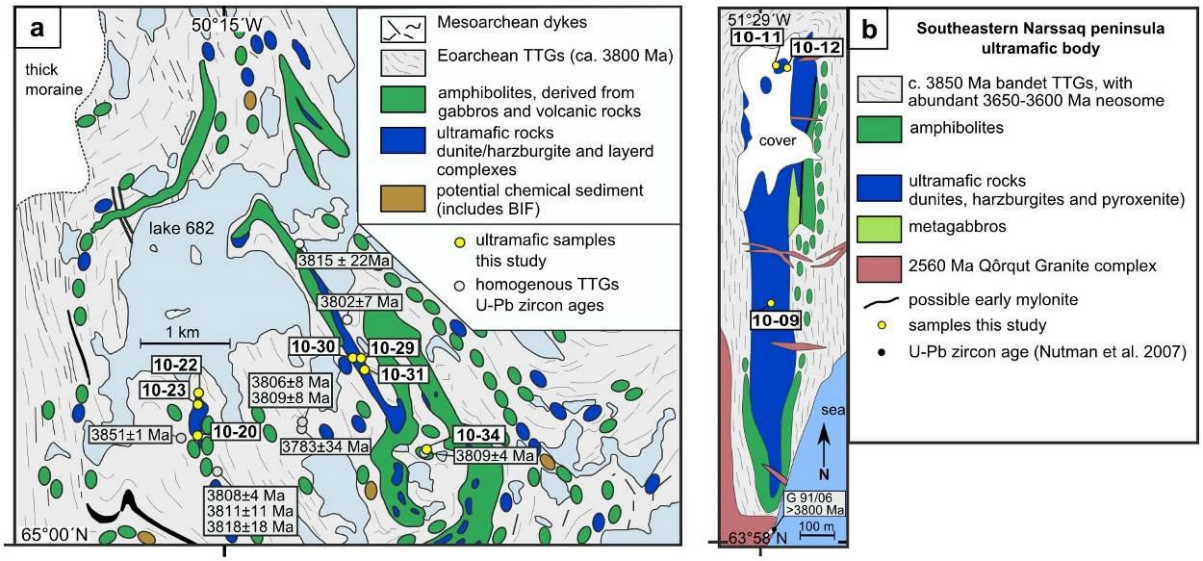

Figure DR1 Simplified geological maps of the locations SOISB and NUB indicated in Fig. 1 **a**, Simplified map of the region south of Isua Supracrustal Belt (SOISB) after Nutman et al. (2009); **b**, Simplified map of the Narssaq Complex after Nutman et al. (2007). Age data are compiled from Amelin et al. (2010) and Nutman et al. (1996; 1999; 2007, 2009). Sample numbers in both maps refer to sample localities of this study.

The eight SOISB samples selected for this study are all massive spinel-peridotites with a mineral composition dominated by olivine and variable amounts of orthopyroxene, amphibole, and opaque phases. Occasionally, serpentine, chlorite, biotite and sulphides occur. Secondary phases like amphibole, serpentine, chlorite, biotite and magnetite in part modifying the primary mineral composition. Except for samples 10-20C and 10-23, the peridotites contain small grains of picotite or hercynite, commonly rimmed by magnetite. Two of the samples have >90% of olivine, thus classifying them as dunites (10-22 and 10-23). Six of the

SOISB peridotites display a harzburgitic mineralogy that was slightly modified by secondary metamorphic and metasomatic overprint. During this processes, pyroxene was replaced by amphibole to variable extents. Amphibole occurs as single grains overgrowing olivine and/or orthopyroxene (Fig. DR2 a-b) or as patches of anhedral grains (Fig. DR2 c-d). One sample (10-34) contains clinopyroxene. While amphibole grew during amphibole facies metamorphism, serpentine, chlorite, biotite and magnetite indicate later low temperature alteration.

Fo# obtained for olivine from SOISB peridotites range from 87 to 92, with the dunites displaying higher Fo# of 91 and 92 and the other peridotites Fo# between 87 and 91, respectively (Table DR1). The Fo# below 89 obtained from SOISB peridotites may indicate Mg-Fe redistribution in olivine during early melt-rock interaction or modification during amphibolite facies metamorphism. Magnetite was formed during metamorphism and/or late serpentinisation and the spinel composition was altered during metamorphism towards more Al-rich compositions. Hence, spinel is not suited to distinguish between a mantle and a magmatic cumulate origin of these peridotites.

Based on petrographic observations of their microstructure, the SOISB peridotites can be divided into two groups, which also correspond to groups 1 and 2 as distinguished based on the PGE abundances of the samples as described in the main text of the manuscript.

Group 1 peridotites (10-20C, 10-22, 10-23 and 10-34) are characterized by a coarse-grained microstructure that was likely only little recrystallized during post-magmatic metamorphic events (Fig. DR2 a-b). Olivine in group 1 peridotites is primary whereas group 2 peridotites show variable degrees of recrystallization as indicated by sub-equigranular olivine the mineral assemblages (Fig DR2 c-d). Of the four group 2 samples, 10-29A and 10-29B show a low proportion of recrystallized olivine and a predominantly medium- to coarse-grained microstructure. Conversely, samples 10-30 and 10-31 from group 2 display a predominantly fine to medium-grained microtexture and higher proportions of recrystallized

olivine. Group 2 samples are clearly discernible from group 1 peridotites based on their primitive mantle-normalized PGE-Re patterns (see description in the main text of the manuscript).

Samples from the Narssaq Peninsula

The Narssaq ultramafic body (Fig. DR1 b) was described by Nutman et al. (2007). Large parts of the Narssaq ultramafic body are highly deformed and altered, showing, e.g., interaction of younger pegmatites with ultramafic rock assemblages. However, some parts, especially at the northern end of the body, are well preserved and show primary structures like dunite dikes and recrystallized pyroxenite dykes, which now contain amphibole and phlogopite. Peridotites from these localities contain pristine olivine that occasionally displays undulose extinction zones (Fig. DR2 e-f). Referring to unpublished data, Nutman et al. (2007) stated that dunites from the north of the Narssaq ultramafic body have chemical characteristics of strongly depleted upper mantle peridotites. In the three selected massive, coarse-grained peridotites (10-09, 10-11 and 10-12B) olivine is the dominant phase. Additional phases are orthopyroxene, amphibole and spinel (Fig. DR2 g-h). Occasionally, chlorite occurs intergrown with amphibole. Sample 10-11 displays a dunitic mineral assemblage (yielding olivine content over 90%). The three Narssaq peridotites display a similarly coarse-grained microstructure comparable to those of group 1 peridotites from SOISB. Samples 10-09 and 10-11 are crosscut by thin serpentine veins that are less abundant in sample 10-12B and in SOISB group 1 samples. Sample 10-12B contains more amphibole and traces of biotite than the other Narssaq samples. In contrast to the other peridotites, 10-12B contains small amounts of ferro-actinolite beside hornblende. All Narssaq peridotites are rich in magnetite and also contain small grains of chromite, commonly rimmed by magnetite. For the Narssaq samples, no pristine spinel occurs to be used as discrimination criteria for a potential mantle origin as by Friend et al. (2002) and Rollinson (2007). Spinel show high Cr#

(Cr#= 100* molar (Cr/(Cr+Al)) > 60) and low Mg# (Mg#= 100* molar (Mg/(Mg+Fe)) < 40) and plot on the metamorphic trend in the Cr# vs. Mg# diagram of Haggerty (1991). Olivine is Mg-rich with essentially constant Fo# between 91 and 92.

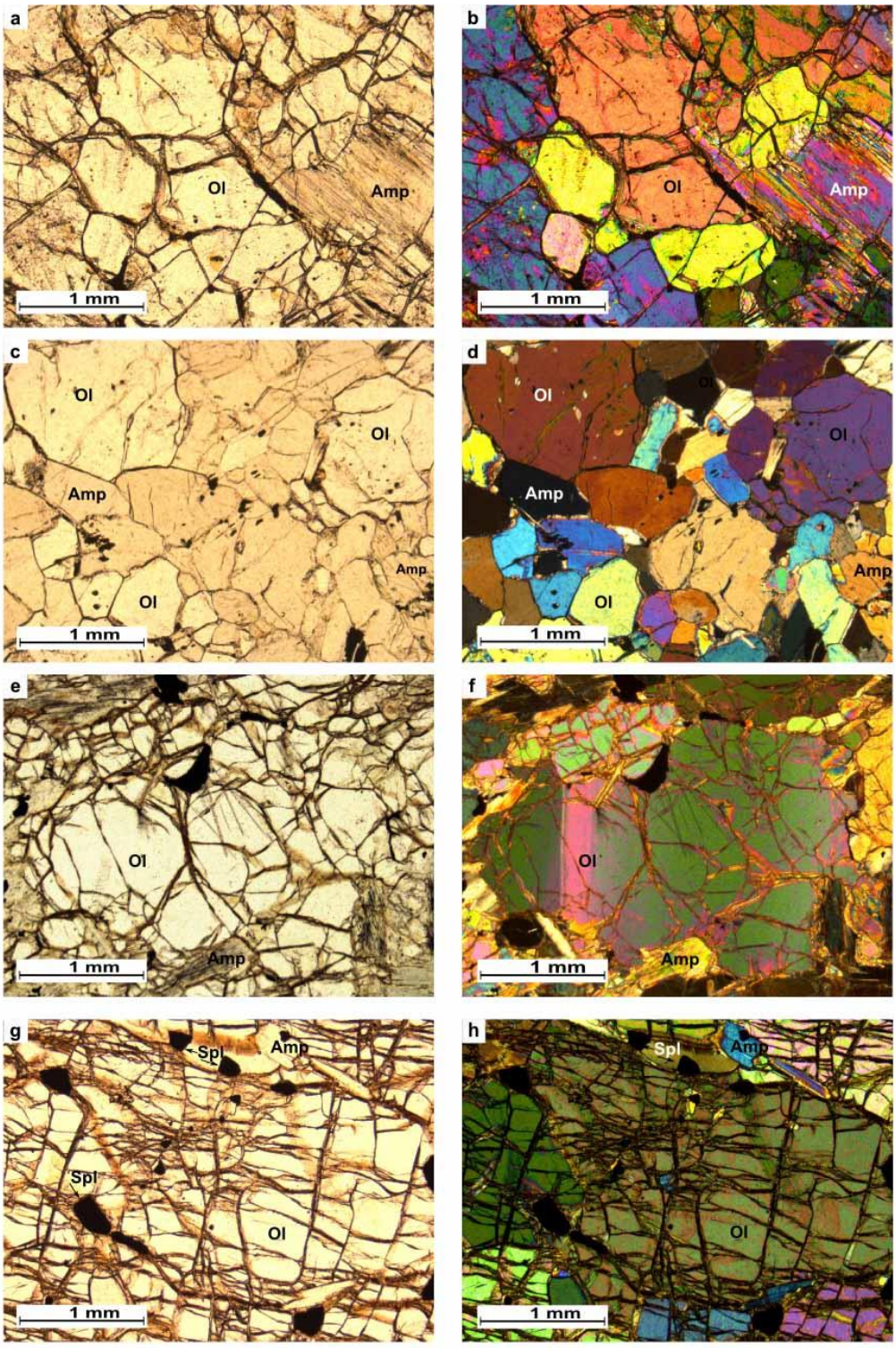

Figure DR2 Microphotographs illustrating the different textures of the peridotites, a, c, e, g are in plane-polarised light and b, d, f, h cross polarised light. a-b, type 1 coarse-grained peridotite from SOISB (10-20C) with Amp overgrow; c-d, type 2 partially re-crystallized -peridotite from SOISB (10-

29B); e-f, undulose extinction in olivine, sample from Narssaq ultramafic body; g-h, group 1 coarse-grained dunite from Narssaq ultramafic body (10-11) crosscut by fine serpentine veins. Ol: olivine, Amp: amphibole, Spl: spinel.

Major and minor element compositions

The whole rock Mg/Si and Al/Si ratios obtained from the Narssaq Complex peridotites range from 1.24 to 1.53 and 0.0253 to 0.0551, respectively (Table DR1). The four peridotites of SOISB group 1 show a similar range of Mg/Si and Al/Si ratios from 1.11-1.50 and 0.0106-0.0632, respectively (Table DR1). The SOISB group 2 peridotites yield higher Al/Si ratios ranging from 0.0939 to 0.175, and lower Mg/Si ranging from 0.871x to 1.19 (Table DR1). As expected for peridotites, MgO is negatively correlated with SiO_2, Al_2O_3, CaO and TiO_2 and positively correlated with NiO (Fig. DR3). The correlations described are typical for melt residues and they commonly result from a combination of melt extraction and processes like melt infiltration (Palme and O'Neill, 2014). Group 1 peridotites show Mg# (Mg# = molar (Mg/(Mg+Fe))*100) between 88 and 90 except for sample 10-20C, with Mg# 85. The Mg# obtained from group 2 peridotites range from 84 to 88, respectively (Table DR1).

The scatter of a few group 2 samples in, e.g., CaO versus SiO_2 space likely reflects secondary processes like melt-rock interaction or disturbance during post-magmatic metasomatic events, as also indicated by amphibole overgrowing other minerals (Fig. DR2 c-d) and by the occurrence of chlorite and serpentine veins.

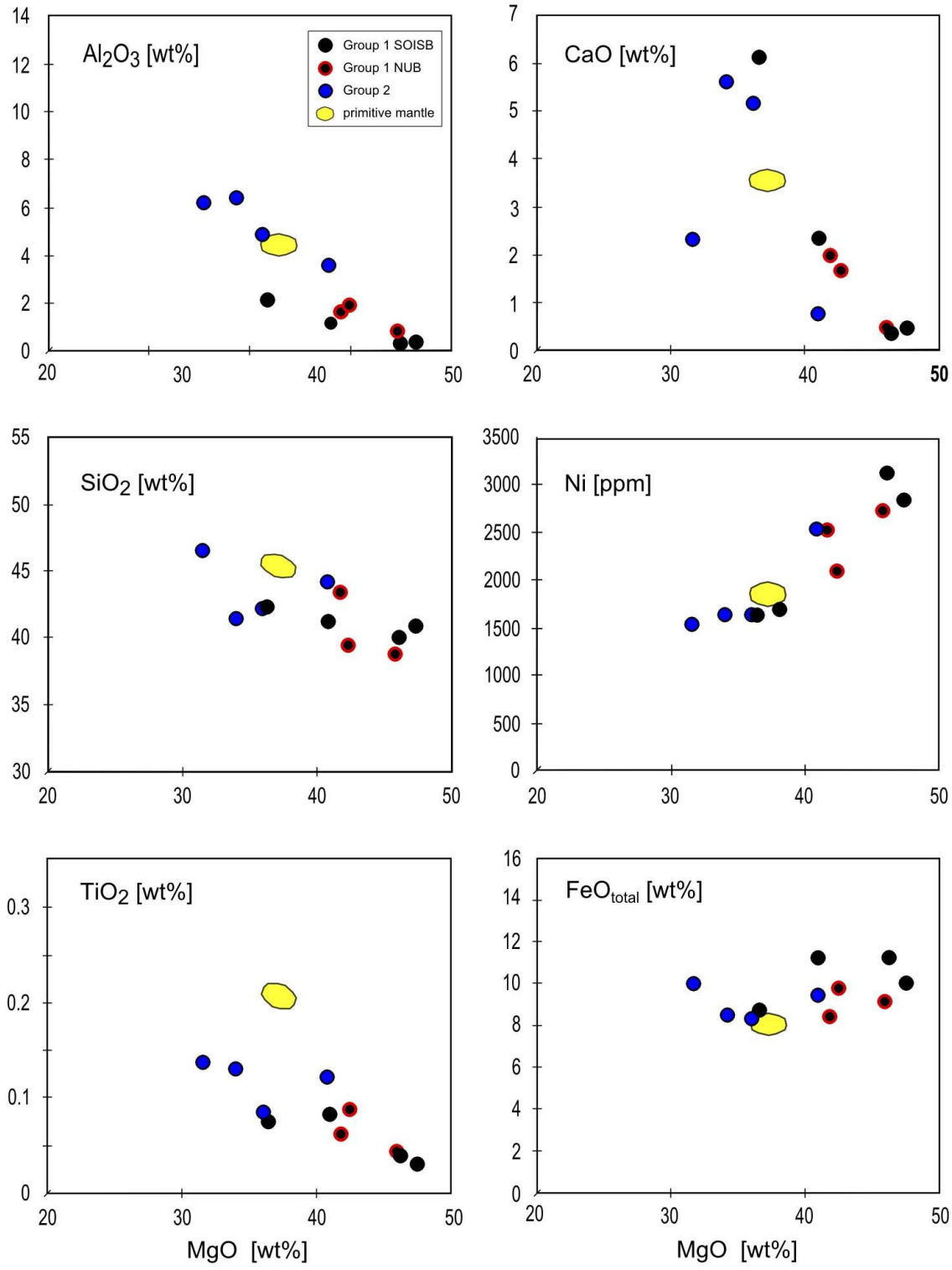

Figure DR3 Variation diagrams showing Al_2O_3, CaO, SiO_2, Ni, TiO_2 and FeO_{total} versus MgO. Primitive mantle values are from McDonough and Sun (1995) and Palme and O´Neill (2014).

PGE-Re abundances

IPGE variations

Group 1 peridotites show minor fractionation between IPGEs, this is common in peridotites because these elements are mainly controlled by residual alloys (“nugget effect”), once high degrees of partial melting lead to full exhaustion of sulphur (Mungall and Brenan, 2014). Therefore, the absolute abundances of IPGE are not only somewhat variable due to redistribution during melt infiltration processes, but can also have an influence on the reproducibility of IPGE. Since IPGEs alloys are occasionally heterogeneously distributed in the sample powders and IPGE abundances obtained from different powder fractions may vary and result in non-representative, minor variations in Os/Ir, Ir/Ru, Ru/Os ratios (Lorand et al., 2013; Aulbach et al., 2016). Alternatively, PGE patterns with positive Ru and negative Ir anomalies similar to group 1 samples could be ascribed to chromite accumulation as it is observed in layered intrusions or cumulates of komatiite flows (Puchtel et al., 2009; Coggon et al., 2015). However, field relationships and petrography clearly indicate that chromite cumulates are absent in these rocks and komatiite flows are also not found in western Greenland.

Coggon et al. (2015) reported PGE patterns of meta-peridotites and chromitites from the Ujaragssuit Nunât layered ultramafic body and nearby ultramafic enclaves, showing clear evidence for magmatic chromitite accumulation (Fig. DR4). All but one of these samples display negative Ir anomalies and positive Ru anomalies. Based on low magnitude positive anomalies in Os and Ru relative to Ir, Coggon et al. (2015) concluded that the IPGE budget was not only controlled by chromite and/or any chromite-hosted PGM, but at least one further phase that exerted a control on IPGE fractionation. Ujaragssuit Nunât meta-peridotites show distinct, negative Pt anomalies relative to Pd. This contrasts with the peridotites of this study, where this is far less distinct or absent (Fig. DR4). Our samples do not show a positive correlation of Os concentrations versus Os/Pt ratios as reported for the Ujaragssuit Nunât

whole-rock samples. In addition, no correlation exists between PGEs and Al_2O_3, (e.g. Os/Ir versus Al_2O_3 (Fig. DR5 a), Ru and Cr (e.g., Locmelis et al. 2011; Fig. DR5 b), amount of Cr-Spinel with Pt/Os ratios (Coggon et al. 2015), and Os/Ir versus Os (Fig. DR5 c), supporting our conclusion that the IPGE contents in the investigated samples were not controlled by chromite accumulation

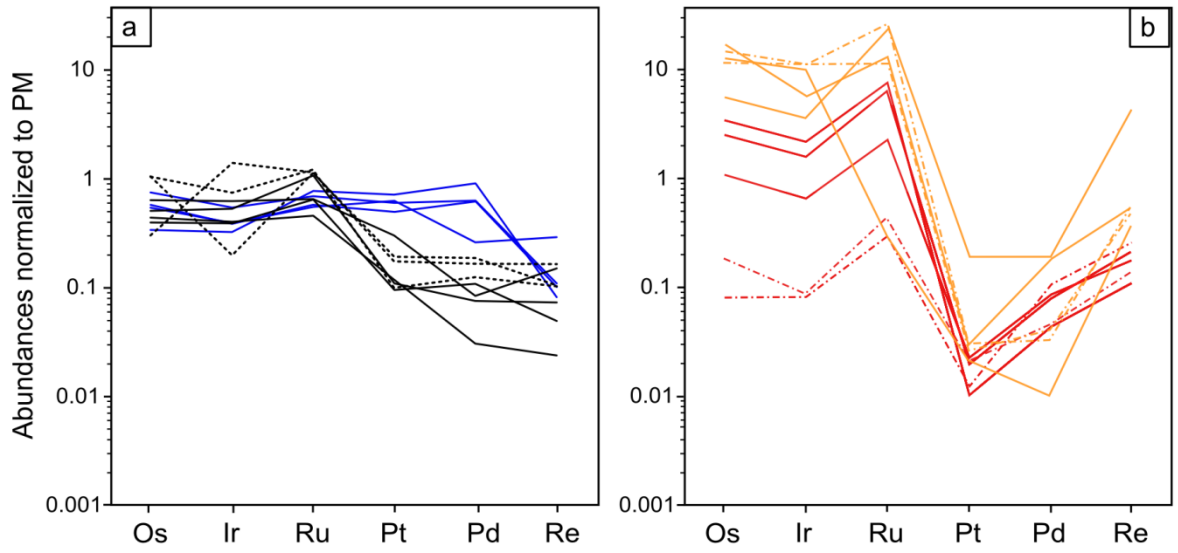

Figure DR4 Primitive mantle-normalized platinum-group-element patterns of Eoarchean dunites and harzburgites from southern west Greenland. **a**, solid black lines are SOISB group 1 peridotites, stippled black lines represent NUB group 1 peridotites, blue lines represent group 2 peridotites; **b**, red solid lines meta-peridotites from the Ujaragssuit Nunât layered ultramafic body (Coggon et al. 2015) and stippled red lines meta-peridotites from peridotite enclaves in the vicinity of the Ujaragssuit Nunât layered ultramafic body (Coggon et al. 2015), solid orange lines chromitites from the Ujaragssuit Nunât layered ultramafic body (Coggon et al. 2015) and stippled orange from peridotite enclaves in the vicinity of the Ujaragssuit Nunât layered ultramafic body (Coggon et al. 2015).

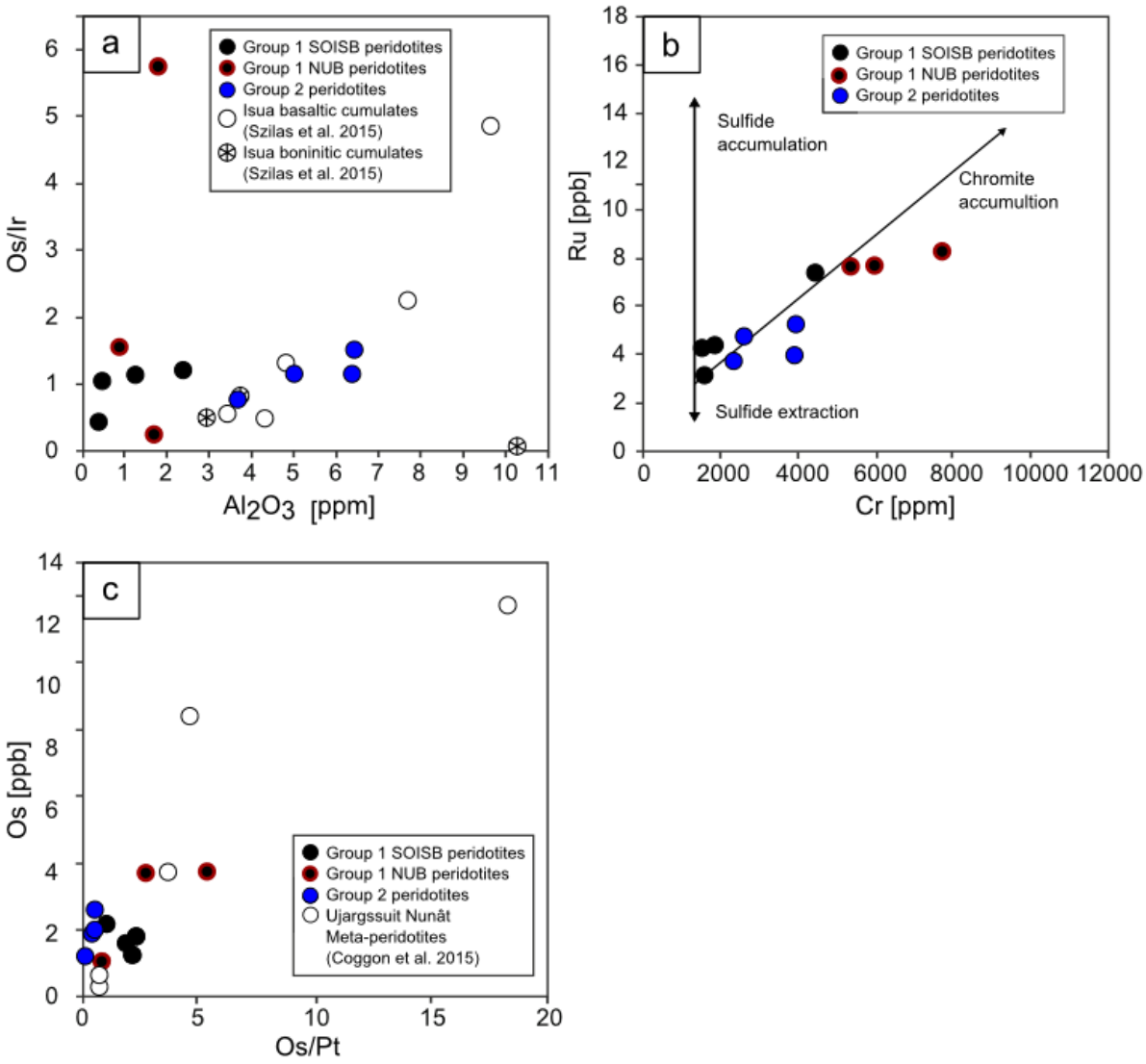

Figure DR5 a, Os/Ir versus Al_2O_3 concentration; open symbol mafic cumulates from the Isua Supracrustal Belt (Szilas et al. 2015); **b**, Ru concentration versus Cr, chromite accumulation and sulfide accumulation and extraction trend after Locmelis et al. (2011); **c,** Os versus Os/Pt; open symbols Ujaragssuit Nunât layered ultramafic body meta-peridotite and from peridotite enclaves in the vicinity (Coggon et al. 2015).

Szilas et al. (2015) reported PGE pattern obtained from ultramafic rocks from the Isua Supracrustal Belt, and characterized them as basaltic and boninitic cumulates. Samples of Szilas et al. (2015) yielding cumulate PGE signature are shown for comparison in figure DR6. Moreover, group 1 peridotite IPGE abundances are in the range of the Balmuccia dunites and harzburgites (Fig.3, DR7a) and ophiolitic harzburgites and dunites (Becker and Dale et al., 2016) e.g. Shetland Ophiolite (UK) (Fig. DR7b) (O´Driscoll et al., 2012).

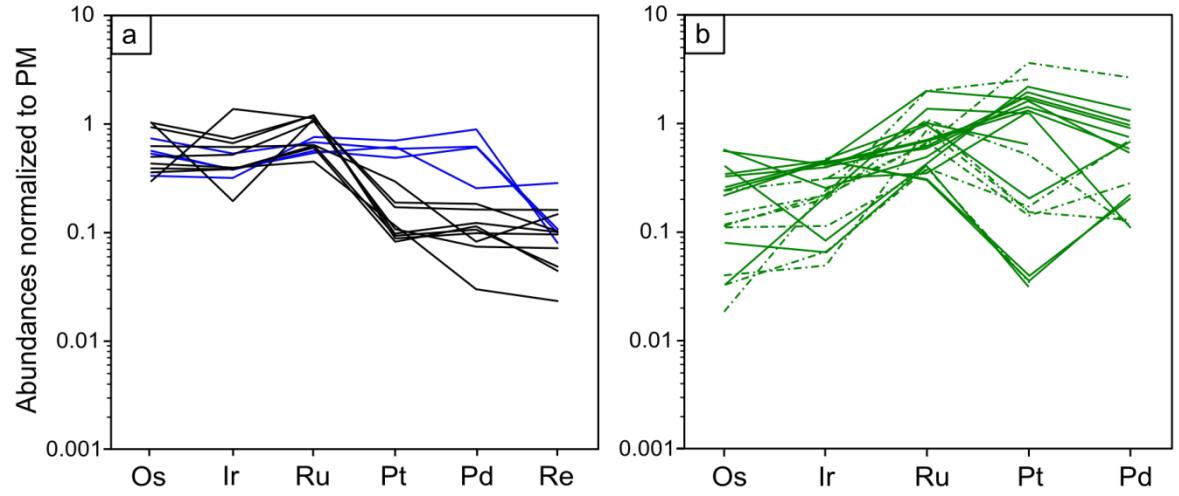

Figure DR6 Primitive mantle-normalized platinum-group-element patterns of Eoarchean dunites and harzburgites from southern West Greenland examined in this study. **a**, Black lines are SOISB group 1 peridotites, stippled black lines represent NUB group 1 peridotites, blue lines represent group 2 peridotites; **b**, solid green lines Isua Supracrustal Belt basalt cumulates (Szilas et al., 2015) and stippled green lines Isua boninitic cumulates (Szilas et al. 2015).

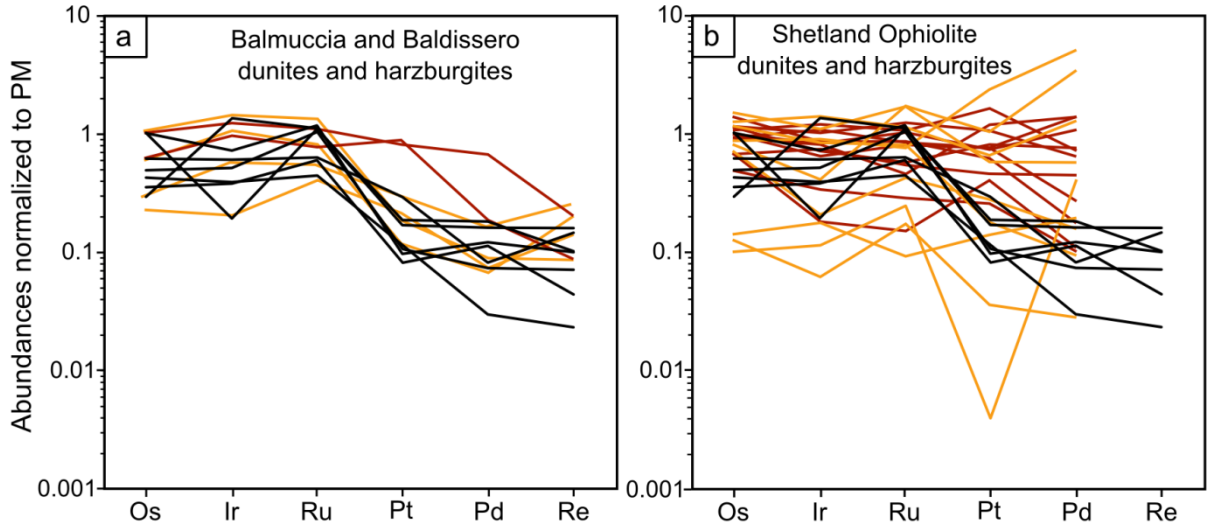

Figure DR7 Primitive mantle -normalized platinum-group-element (PGE) patterns of Eoarchean dunites and harzburgites from southern West Greenland examined in this study. Black lines are SOISB group 1 peridotites, red lines represent harzburgites and orange lines dunites from, **a**, Balmuccia (Wang et al., 2013); **b**, Shetland ophiolite (UK) (O´Driscoll et al., 2012).

PPGE refertilization and disturbance of Re-Os systematics

The different Re-depletion ages combined with re-enriched PPGE and higher Al/Si ratios of group 2 suggest a multistage evolution history for the peridotites, comprising melt depletion and interaction with infiltrating melt at upper mantle level and presumably also later alteration in the crust likely associated to metamorphic events. Co-precipitation of sulphides and Al-phases (e.g. pyroxene and spinel) during interaction of percolating melt and peridotite in the lherzolith stability field can account for the re-enriched PPGE and Al (e.g. Becker and Dale, 2016). Alternatively, fluid-rock interaction during amphibole facies metamorphism can cause enrichment of aluminium in ultramafic rocks up to wt% levels (Rosing and Rose, 1993). Group 2 peridotites contain biotite indicative for metasomatic processes. Relative enrichment of PPGEs combined with low Re abundances and varying Re depletion ages (1.66-3.54 Ga) indicate a decoupling of PPGEs and Re during later metasomatic disturbance of the ^{187}Re-^{187}Os decay system, such ages are possibly related to terrane assembly. Alternatively, early Archean melt-rock interaction at upper mantle conditions involving melt from Re-depleted sources may also explain the observed re-enrichment of PPGEs of group 2 samples. Chondritic normalized Pd/Ir and Pt/Ir ratios of three group 2 samples are positive correlated with Al_2O_3 and Re/Os isotopic composition and negative with MgO, indicates that these PGE ratios might be modified by interaction with melts (Pearson et al., 2004).

In addition, Re can be mobilized easily during later disturbance and during recent weathering. Hence, the young Re-depletion ages may reflect artefacts and have therefore no geological relevance.

Bennett et al. (2002) reported Re-Os isotope data for four peridotites from SOISB. One peridotite of their suite of samples was collected from the same ultramafic unit as group 2 samples (10-29A and B, 10-30 and 10-31; Fig. DR1). As discussed above, group 2 peridotites show indications for later metasomatic disturbance of the Re–Os isotopic system and nearly

flat PGE patterns, with some variability in Pd and Re. Thus, care must be taken for the interpretation of Re-Os data obtained from group 2 peridotites.

Several initial Os isotope compositions obtained for group 1 peridotites are unrealistically low and reveal over-correction of radiogenic ingrowth due to young addition of Re (Fig. DR8).

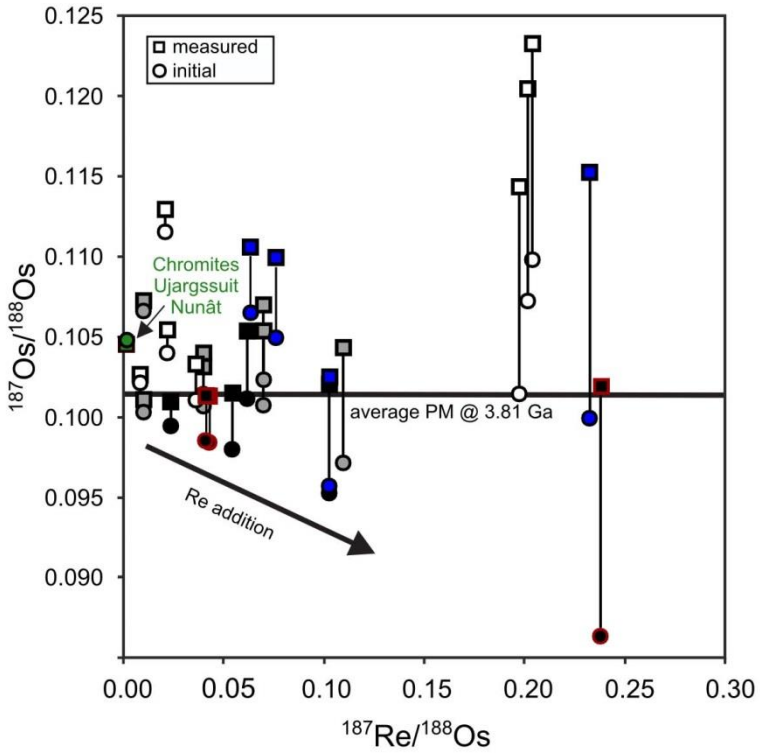

Figure DR8 $^{187}Os/^{188}Os$ versus $^{187}Re/^{188}Os$ isotope diagram showing measured and initial Os isotope compositions after Bennett et al. (2002). The measured $^{187}Os/^{188}Os$ obtained from group 1 peridotites overlap with those of PM (Meisel et al., 2001) recalculated to 3.81 Ga. The initial Os isotope compositions are unrealistically low and reveal over-correction of radiogenic ingrowth due to young addition of Re. Open symbols are literature data from Bennett et al. (2002), and grey symbols Frei and Jensen (2003, ultramafic rocks ISB with Re <200 ppt). The Ujargssuit Nunât layered intrusion data are taken from Bennett et al. (2002), Frei and Jensen (2003) and Coggon et al. (2013) green symbols. Black symbols represent SOISB group 1 peridotites, black symbols with red frame are NUB group 1 peridotites, and blue symbols group 2 peridotites.

The isochron diagram (Fig. DR9) shows as well that some Re was added recently, however, not influencing significantly the Os isotope composition of these samples which remains near to primitive mantle at 3.81 Ga.

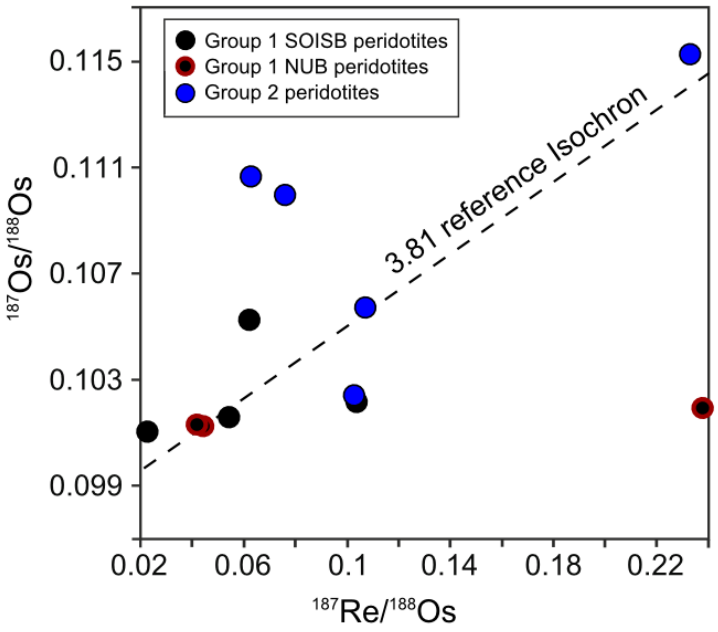

Figure DR9 Re-Os Isochron diagram for group 1 with reference 3.81 Isochron using ^{187}Re decay constant $\lambda = 1.666 \times 10^{-11}$ year^{-1} (Smoliar et al., 1996).

As mentioned above, three samples were processed differently, avoiding all contact with metal tools, and a piece of the jaw breaker were analysed in order to evaluate potential metal contamination. As listed in Table DR2, the results are very similar and do not hint toward significant contamination by unrelated PGE during the first analytical session. The results are not consistently lower for these samples than for those analysed in the first analytical session, where the samples were crushed in a jaw breaker. Os and Ir concentrations were reproduced (discrepancies of < 4%) for sample 10-12B, Pt for sample 10-31 (discrepancies 1.9%) and some HSE were even clearly enrich in some "metal-free" aliquots. Pd and Re were significantly enriched in 10-20C-II and Ir and Ru in 10-31-II. Hence, sample heterogeneity has a major impact on slightly different PGE abundances. This is very common for these types of depleted peridotites. In addition, the reference material (harzburgite MUH-1) show

similar concentration variations for Ir, Pt, Pd and Re, indicating likewise sample heterogeneity. Moreover, the amount rock pulverized is an imported factor. For the first set, powder between 500-1000g rocks were processed, the available rock material for the "metal-free" aliquots was limited (between 30 and 100g). Thus, higher effects of sample heterogeneity were expected and seen in the data obtained from the "metal-free" set, especially regarding elements with low concentrations, e.g. Pt and Pd.

Recent Re addition, as indicated by the isochron diagram (Fig. DR9) may be likely, however, it is not clear if Re was introduced by the jaw crusher steel or by recent weathering and Re mobility, because the newly prepared samples were not in contact to steel and show also a re-enrichment of Re.

Even though, contamination by jaw-breaker-metal cannot be ruled out completely, the difference in primitive mantle normalized PGE pattern between Group 1 and 2 are still clear. The unradiogenic Os isotopic composition and reproduced $^{187}Re/^{188}Os$ and $^{187}Os/^{188}Os$ ratios (e.g. 10-30 II) support the assumption that the potential jaw-breaker-metal contamination was low.

Supplementary Information to Figure 3

The compilation of PGE and Re abundances of Phanerozoic dunitic and harzburgitic peridotites shown in Figure 3 as comparison to the Eoarchean peridotites are taken from Rehkämper et al. (1997 and 1999), Pearson et al. (2004), Luguet et al. (2007), Fischer-Gödde et al. (2011) and Wang et al. (2013). All of these samples are discussed in context of their tectonic setting by Becker and Dale (2016).

SUPPLEMENTARY REFERENCES

Amelin, Y., Kamo, S.L., Lee, D.-C, 2010, Evolution of Early Crust in Chondritic or Non-Chondritic Earth Inferred from U–Pb and Lu–Hf Data for Chemically Abraded Zircon from the Itsaq Gneiss Complex, West Greenland: Canadian Journal of Earth Sciences, v. 48, p. 141–160.

Aulbach, S., Mungall, J.E. and Pearson, D.G., 2016, Distribution and Processing of Highly Siderophile Elements in Cratonic Mantle Lithosphere: Reviews in Mineralogy and Geochemistry, v. 81, p. 239–304, doi:10.2138/rmg.2016.81.5

Becker, H. and Dale, C.W., 2016, Re–Pt–Os Isotopic and Highly Siderophile Element Behavior in Oceanic and Continental Mantle Tectonites: Reviews in Mineralogy and Geochemistry, v. 81, p. 369–440, doi:10.2138/rmg.2016.81.7

Bennett, V.C., Nutman, A.P. and Esat, T.M., 2002, Constraints on mantle evolution from 187Os/ 188Os isotopic compositions of Archean ultramafic rocks from southern West Greenland (3.8 Ga) and Western Australia (3.46 Ga): Geochimica et Cosmochimica Acta, v. 66, p. 2615–2630.

Coggon, J.A., Luguet, A., Fonseca, R.O.C., Lorand, J.-P., Heuser, A. and Appel, P.W.U., 2015, Understanding Re–Os systematics and model ages in metamorphosed Archean ultramafic rocks: A single mineral to whole-rock investigation: Geochimica et Cosmochimica Acta, v. 167, p. 205–240, doi:10.1016/j.gca.2015.07.025

Coggon, J. A., Luguet, A., Nowell, G. M. and Appel, P. W. U., 2013, Hadean Mantle Melting Recorded by Southwest Greenland Chromitite ^{186}Os Signatures. Nature Geosci v. 6(10), p. 871–874.

Cohen, A.S. and Waters, F.G., 1996, Separation of osmium from geological materials by solvent extraction for analysis by thermal ionisation mass spectrometry: Analytica Chimica Acta, v. 332, p. 269–275, doi:http://dx.doi.org/10.1016/0003-2670(96)00226-7

Dziggel, A., Diener, J.F.A., Kolb, J. and Kokfelt, T.F., 2014, Metamorphic Record of Accretionary Processes during the Neoarchaean: The Nuuk Region, Southern West Greenland. Precambrian Research, v. 242, p. 22–38, https://doi.org/10.1016/j.precamres.2013.12.010

Dziggel, A., Kokfelt, T.F., Kolb, J., Kisters, A.F.M. and Reifenröther, R., 2017, Tectonic Switches and the Exhumation of Deep-Crustal Granulites during Neoarchean Terrane Accretion in the Area around Grædefjord, SW Greenland. Precambrian Research v. 300, p. 223–245, https://doi.org/10.1016/j.precamres.2017.07.027

Fischer-Gödde, M., Becker, H., and Wombacher, F., 2011, Rhodium, gold and other highly siderophile elements in orogenic peridotites and peridotite xenoliths: Chemical Geology, v. 280, p. 365–383, https://doi.org/10.1016/j.chemgeo.2010.11.024.

Frei, R., and Jensen K.B., 2003, Re–Os, Sm–Nd Isotope- and REE Systematics on Ultramafic Rocks and Pillow Basalts from the Earth's Oldest Oceanic Crustal Fragments (Isua Supracrustal Belt and Ujaragssuit Nunât Area, W Greenland): Highly Siderophile Elements in the Earth and Meteorties: A Volume in Honor of John Morgan, v. 196, p. 163–191.

Friend, C., Bennett, V. and Nutman, A., 2002, Abyssal peridotites >3,800 Ma from southern West Greenland: field relationships, petrography, geochronology, whole-rock and mineral chemistry of dunite and harzburgite inclusions in the Itsaq Gneiss Complex: Contributions to Mineralogy and Petrology, v. 143, p. 71–92, https://doi.org/10.1007/s00410-001-0332-7

Friend, C. R. L. and Nutman, A. P., 2010, Eoarchean Ophiolites? New Evidence for the Debate on the Isua Supracrustal Belt, Southern West Greenland. American Journal of Science, v. 310(9), p. 826–861, https://doi.org/10.2475/09.2010.04

Haggerty, S.E., 1991, Oxide mineralogy of the upper mantle: Reviews in Mineralogy and Geochemistry, v. 25, p. 355–416.

Hanmer, S. and Greene, D.C., 2002a, A Modern Structural Regime in the Paleoarchean (~3.64 Ga); Isua Greenstone Belt, Southern West Greenland. Tectonophysics 346(3): 201–222, https://doi.org/10.1016/S0040-1951(02)00029-X

Hanmer, S., Hamilton, M.A., Crowley, J.L., 2002b, Geochronological Constraints on Paleoarchean Thrust-Nappe and Neoarchean Accretionary Tectonics in Southern West Greenland. Tectonophysics v. 350(3), p. 255–271, https://doi.org/10.1016/S0040-1951(02)00120-8

Hoffmann, J.E., Münker, C., Polat, A., König, S., Mezger, K., Rosing, M.T., 2010, Highly Depleted Hadean Mantle Reservoirs in the Sources of Early Archean Arc-like Rocks, Isua Supracrustal Belt, Southern West Greenland. Geochimica et Cosmochimica Acta 74(24): 7236–7260, 7236–7260, https://doi.org/10.1016/j.gca.2010.09.027

Hoffmann, J.E., Münker, C., Næraa, T., Rosing, M.T., Herwartz, D., Garbe-Schönberg, D., Svahnberg, H., 2011, Mechanisms of Archean Crust Formation Inferred from High-Precision {HFSE} Systematics in {TTGs}. Geochimica et Cosmochimica Acta 75(15): 4157–4178, https://doi.org/http://dx.doi.org/10.1016/j.gca.2011.04.027

Jenner, F.E., Bennett, V.C., Nutman, A.P., Friend, C.R.L., Norman, M.D., Yaxley, G., 2009. Evidence for Subduction at 3.8 Ga: Geochemistry of Arc-like Metabasalts from the Southern Edge of the Isua Supracrustal Belt. The Application and Interpretation of Micro-Analytical Data, *in* Geochronological Systems, v. 261(1–2), p. 83–98, https://doi.org/10.1016/j.chemgeo.2008.09.016

Komiya, T., Yamamoto, S., Aoki, S., Sawaki, Y., Ishikawa, A., Tashiro, T., Koshida, K., Shimojo, M., Aoki, K., Collerson, K.D., 2015. Geology of the Eoarchean, > 3.95 Ga, Nulliak Supracrustal Rocks in the Saglek Block, Northern Labrador, Canada: The Oldest Geological Evidence for Plate Tectonics: Tectonophysics, v. 662, p.40–66, https://doi.org/10.1016/j.tecto.2015.05.003

Locmelis, M., Pearson, N.J., Barnes, S.J., Fiorentini, M.L., 2011, Ruthenium in komatiitic chromite: Geochimica et Cosmochimica Acta, v. 75, p. 3645-3661.

Lorand, J.-P., Luguet, A. and Alard, O., 2013, Platinum-group element systematics and petrogenetic processing of the continental upper mantle: A review: Lithos, v. 164–167, p. 2–21, doi:http://dx.doi.org/10.1016/j.lithos.2012.08.017

Luguet, A., Shirey, S.B., Lorand, J.-P., Horan, M.F. and Carlson, R.W., 2007, Residual platinum-group minerals from highly depleted harzburgites of the Lherz massif (France) and their role in {HSE} fractionation of the mantle: Geochimica et Cosmochimica Acta, v. 71, p. 3082–3097, doi:http://dx.doi.org/10.1016/j.gca.2007.04.011

McDonough, W.F. and Sun, S.-S., 1995, The composition of the Earth: Chemical Geology, v. 120, p. 223–253.

Meisel, Thomas, Richard J. Walker, Anthony J. Irving, and Jean-Pierre Lorand, 2001, Osmium Isotopic Compositions of Mantle Xenoliths: A Global Perspective: Geochimica et Cosmochimica Acta, v. 65, p. 1311–1323, http://dx.doi.org/10.1016/S0016-7037(00)00566-4

Meisel, T. and Horan, M.F., 2016, Analytical Methods for the Highly Siderophile Elements. Reviews in Mineralogy and Geochemistry, v. 81, p. 89–106, doi:10.2138/rmg.2016.81.02

Mungall, J.E. and Brenan, J.M., 2014, Partitioning of platinum-group elements and Au between sulfide liquid and basalt and the origins of mantle-crust fractionation of the chalcophile elements: Geochimica et Cosmochimica Acta, v. 125, p. 265–289. doi:http://dx.doi.org/10.1016/j.gca.2013.10.002

Næraa, T., Schersten, A., Rosing, M.T., Kemp, A.I.S., Hoffmann, J.E., Kokfelt, T.F., and Whitehouse, M.J., 2012, Hafnium isotope evidence for a transition in the dynamics of

continental growth 3.2 Gyr ago: Nature, v. 485, p. 627–630, https://doi.org/10.1038/nature11140.

Nutman, A.P., McGregor, V.R., Friend, C.R.L., Bennett, V.C. and Kinny, P.D., 1996, The Itsaq Gneiss Complex of Southern West Greenland; the World's Most Extensive Record of Early Crustal Evolution (3900-3600 Ma): Precambrian Research, v. 78, p. 1–39, http://dx.doi.org/10.1016/0301-9268(95)00066-6

Nutman, P. Allen, C. Vickie Bennett, L. Clark R. Friend, and D. Marc Norman, 1999, Meta-Igneous (Non-Gneissic) Tonalites and Quartz-Diorites from an Extensive Ca. 3800 Ma Terrain South of the Isua Supracrustal Belt, Southern West Greenland: Constraints on Early Crust Formation: Contributions to Mineralogy and Petrology, v. 137, p. 364–388, http://dx.doi.org/10.1007/s004100050556

Nutman, A.P., Friend, C.R.L., Horie, K. and Hidaka, H., 2007, The Itsaq Gneiss Complex of Southern West Greenland and the Construction of Eoarchaean Crust at Convergent Plate Boundaries, *in* Martin J. van Kranendonk, R.H.S. and Bennett, V.C., eds., Earth's Oldest Rocks: Developments in Precambrian Geology 15, Elsevier, p. 187–218.

Nutman, A.P., Bennett, V.C., Friend, C.R.L., Jenner, F., Wan, Y. and Liu, D., 2009, Eoarchaean crustal growth in West Greenland (Itsaq Gneiss Complex) and in northeastern China (Anshan area): review and synthesis, In: Cawood, P. A. and Kröner, A. eds. Earth Accretionary Systems in Space and Time: Geological Society, London, Special Publications, v. 318, p. 127–154, doi:10.1144/SP318.5

Nutman, A.P., Bennett, V.C., Friend, C.R.L., Hidaka, H., Yi, K., Lee, S.R., Kamiichi, T., 2013, The Itsaq Gneiss Complex of Greenland: Episodic 3900 to 3660 Ma Juvenile Crust Formation and Recycling in the 3660 to 3600 Ma Isukasian Orogeny: American Journal of Science, v. 313(9), p. 877–911.

Nutman, A.P., Bennett, V.C., Friend, C.R.L., 2015, Proposal for a continent "Itsaqia" amalgamated at 3.66 Ga and rifted apart from 3.53 Ga: Initiation of a Wilson Cycle near the start of the rock record: American Journal of Science, v. 315, p. 509–536, https://doi.org/10.2475/06.2015.01

O'Driscoll, B., Day, J.M.D., Walker, R.J., Daly, J.S., McDonough, W.F., Piccoli, P.M., 2012. Chemical heterogeneity in the upper mantle recorded by peridotites and chromitites from the Shetland Ophiolite Complex, Scotland: Earth and Planetary Science Letters, v. 333–334, p.226–237, https://doi.org/10.1016/j.epsl.2012.03.035

Palme, H. and O'Neill, H.S.C., 2014, 3.1 - Cosmochemical Estimates of Mantle Composition, *in* Turekian, K.K., ed., Treatise on Geochemistry (second edition): Elsevier, Oxford, p. 1–39.

Pearson, D.G., Irvine, G.J., Ionov, D.A., Boyd, F.R. and Dreibus, G.E., 2004, Re–Os isotope systematics and platinum group element fractionation during mantle melt extraction: a study of massif and xenolith peridotite suites, Chemical Geology, v. 208, p. 29–59, doi:http://dx.doi.org/10.1016/j.chemgeo.2004.04.005

Polat, A., Hofmann, A.W., Rosing, M.T., 2002, Boninit-like Volcanic Rocks in the 3.7–3.8 Ga Isua Greenstone Belt, West Greenland: Geochemical Evidence for Intra-Oceanic Subduction Zone Processes in the Early Earth: Chemical Geology, v. 184(3–4), p. 231–254, https://doi.org/10.1016/S0009-2541(01)00363-1

Polat, A., and Hofmann, A.W., 2003, Alteration and Geochemical Patterns in the 3.7–3.8 Ga Isua Greenstone Belt, West Greenland: Precambrian Research , v. 126(3–4), p. 197–218,

Polat, A., Hofmann, A.W., Münker, C., Regelous, M., Appel, P.W.U., 2003, Contrasting geochemical patterns in the 3.7–3.8 Ga pillow basalt cores and rims, Isua greenstone belt, Southwest Greenland: implications for postmagmatic alteration processes: Geochimica et Cosmochimica Acta, v. 67, p. 441–457, https://doi.org/10.1016/S0016-7037(02)01094-3

Polat, A., Wang, L., Appel, P.W.U., 2015, A review of Structural Patterns and Melting Processes in the Archean Craton of West Greenland: Evidence for Crustal Growth at Convergent Plate Margins as Opposed to Non-Uniformitarian Models: Tectonophysics, v. 662, p. 67–94, https://doi.org/http://dx.doi.org/10.1016/j.tecto.2015.04.006

Puchtel, I.S., Walker, R.J., Brandon, A.D. and Nisbet, E.G., 2009, Pt–Re–Os and Sm–Nd isotope and HSE and REE systematics of the 2.7 Ga Belingwe and Abitibi komatiites: Geochimica et Cosmochimica Acta, v. 73, p. 6367–6389, doi:10.1016/j.gca.2009.07.022

Rehkämper, M., Halliday, A.N., Barfod, D., Fitton, J.G., Dawson, J.B., 1997, Platinum-Group Element Abundance Patterns in Different Mantle Environments: Science, v. 278, p. 1595–1598. doi:10.1126/science.278.5343.1595

Rehkämper, M., Halliday, A.N., Alt, J., Fitton, J.G., Zipfel, J. and Takazawa, E., 1999, Non-chondritic platinum-group element ratios in oceanic mantle lithosphere: petrogenetic signature of melt percolation?: Earth and Planetary Science Letters, v. 172, p. 65–81, doi:10.1016/S0012-821X(99)00193-4

Rollinson, H., 2007, Recognising early Archaean mantle: a reappraisal: Contributions to Mineralogy and Petrology, v. 154, p. 241–252, doi:10.1007/s00410-007-0191-y

Rosing, M.T. and Rose, N.M., 1993, Fluid-rock Interaction in the Deeper Continental Lithosphere The role of ultramafic rocks in regulating the concentrations of volatile and non-volatile components during deep crustal metamorphism: Chemical Geology, v. 108, p. 187–200, doi:10.1016/0009-2541(93)90324-C

Shirey, S.B., and Walker R.J., 1998, The Re-Os isotope system in cosmochemistry and high-temperature geochemistry: Annual Review of Earth and Planetary Sciences, v. 26, p. 423–500.

Smoliar, M.I, Walker, R.J, Morgan, J.W., 1996, Re–Os ages of group IIA, IIIA, IVA, and IVB iron meteorites: Science, v. 271, p. 1099–1102.

Szilas, K., Kelemen, P.B., Rosing, M.T. The petrogenesis of ultramafic rocks in the > 3.8 Ga Isua supracrustal belt, southern West Greenland: Geochemical evidence for two distinct magmatic cumulate trends. Gondwana Res. 28 565-580 (2015).

Wang, Z., Becker, H. and Gawronski, T., 2013, Partial re-equilibration of highly siderophile elements and the chalcogens in the mantle: A case study on the Baldissero and Balmuccia peridotite massifs (Ivrea Zone, Italian Alps): Geochimica et Cosmochimica Acta, v. 108, p. 21–44, doi:10.1016/j.gca.2013.01.021

SUPPLEMENTARY TABLES

Table DR1: Major and trace element XRF concentrations of peridotites from south of ISB (SOISB) and Narssaq ultramafic body (NUB) and representative Fo# obtained from electron microprobe analyses

		NUB			SOISB							
		10-09	10-11	10-12B	10-20C	10-22	10-23	10-34	10-29A	10-29B	10-30	10-31
Rock		H	D	H	H	D	D	H	H	H	H	H
Latitude	N	63°58,099´	63°58,349´	63°58,351´	65°00,740´	65°00,896´	65°00,921´	65°00,746´	65°00,997´	65°00,997´	65°01,007´	65°00,956´
Longitude	W	51°28,289´	51°28,657´	51°28,656´	50°14,977´	50°15,007´	50°14,992´	50°11,965´	50°12,580´	50°12,580´	50°12,468´	50°12,498´
PGE-group		1	1	1	1	1	1	1	2	2	2	2
SiO_2	[wt%]	39.5	38.8	43.5	41.3	40.9	39.9	42.6	44.2	41.6	42.5	47.0
TiO_2	[wt%]	0.09	0.04	0.06	0.08	0.03	0.04	0.08	0.12	0.13	0.09	0.14
Al_2O_3	[wt%]	1.92	0.87	1.70	1.25	0.38	0.47	2.38	3.67	6.42	5.01	6.38
Fe_2O_3	[wt%]	9.81	9.15	8.43	11.3	10.0	11.2	8.69	9.34	8.34	8.34	10.1
MnO	[wt%]	0.14	0.14	0.13	0.15	0.15	0.16	0.15	0.13	0.13	0.12	0.15
MgO	[wt%]	42.5	45.9	41.8	40.9	47.5	46.2	36.5	40.9	34.2	36.0	31.7
CaO	[wt%]	1.66	0.49	1.99	2.33	0.46	0.40	6.19	0.75	5.61	5.22	2.37
K_2O	[wt%]	<LLD	<LLD	0.01	<LLD	<LLD	<LLD	<LLD	0.07	0.13	0.09	0.21
Na_2O	[wt%]	<LLD	<LLD	<LLD	<LLD	<LLD	<LLD	<LLD	<LLD	0.84	<LLD	<LLD
P_2O_5	[wt%]	<LLD	<LLD	<LLD	<LLD	<LLD	<LLD	<LLD	<LLD	<LLD	<LLD	<LLD
Cr	[ppm]	5996	7720	5397	1834	1549	4432	2627	2344	3914	3973	1642
Ni	[ppm]	2116	2755	2539	2410	2858	3140	1673	2549	1647	1667	1574
LOI	[wt%]	3.73	2.85	1.39	3.23	0.79	0.88	3.48	1.61	2.34	0.82	1.58
Total	[wt%]	100.2	99.1	99.9	100.6	100.4	99.9	100.5	101.3	100.2	99.1	100.3
Mg# *		88.2	89.6	89.5	84.9	89.1	87.7	87.9	88.3	87.6	88.2	84.4
Al/Si		0.0551	0.0253	0.0441	0.0342	0.0106	0.0134	0.0632	0.0939	0.175	0.134	0.154
Mg/Si		1.39	1.53	1.24	1.28	1.50	1.50	1.11	1.19	1.06	1.09	0.871
olivine Fo# **		90.6	91.9	91.5	87.6	91.8	91.0	87.9	89.8	89.7	90.5	87.1

H, harzburgite; D, dunite

*Mg# = 100 x (molar Mg/(Fe_{total} + Mg))

**Fo# = 100 x molar (Mg/(Fe+ Mg))

Table DR2: PGE, Re, Os, Re-Os isotopes and model ages of peridotites from south of ISB (SOISB) and Narssaq ultramafic body (NUB)

NUB	Rock	PGE-group	Os ppb	Ir ppb	Ru ppb	Pt ppb	Pd ppb	Re ppb	$^{187}Re/^{188}Os$	$^{187}Os/^{188}Os$**	γ(Os)i (t=3.80 Ga)	$^{187}Os/^{188}Os(t)$ (t=3.80 Ga)	$T_{Ma(PM)}$ Os(Ga)	$T_{RD(PM)}$ Os(Ga)	$T_{Ma(ch)}$ Os (Ga)	$T_{RD(ch)}$ Os (Ga)
10-09	H	1	3.95	0.679	7.76	1.43	1.31	0.036	0.044(2)	0.1013	-2.3	0.09845	4.1	3.70	4.2	3.79
10-11	D	1	4.00	2.53	8.27	0.73	0.87	0.035	0.042(2)	0.1013	-2.2	0.09857	4.1	3.70	4.2	3.79
10_11 (duplicate)	D	1	3.59	2.29	8.35	0.68	0.71	0.033	0.045(2)	0.1011	-2.5	0.09818	4.2	3.73	4.2	3.81
10-12B	H	1	1.14	4.73	7.75	1.29	1.16	0.056	0.238(6)	0.1019	-14.3	0.08631	8.8	3.62	8.0	3.71
10-12B II*	H	1		4.57	7.68	0.83	0.58	0.017								
SOISB											(t=3.81 Ga)	(t=3.81 Ga)				
10_20C	H	1	2.40	2.09	4.44	2.24	0.59	0.051	0.103(3)	0.1021	-5.3	0.09539	4.8	3.58	4.8	3.68
10_20C II*	H	1	1.92	1.76	2.20	1.67	1.11	0.075	0.189(1)	0.1086	-4.5	0.09625	4.9	2.83	5.0	2.68
10_22	D	1	1.39	1.33	4.27	0.62	0.82	0.016(1)	0.054(5)	0.1016	-2.7	0.09800	4.2	3.67	4.3	3.76
10_22 (duplicate)	D	1	1.51	1.34	4.41	0.70	0.75	0.017(1)	0.054(5)	0.1015	-2.7	0.09795	4.2	3.68	4.3	3.77
10_23	D	1	1.94	1.81	7.39	0.81	0.53(7)	0.025(1)	0.062(4)	0.1052	0.5	0.10117	3.7	3.14	3.8	3.28
10_34	H	1	1.68	1.33	3.13	0.87	0.21(7)	0.008(1)	0.023(4)	0.1010	-1.3	0.09942	4.0	3.75	4.0	3.84
10_29A	h	2	2.82	1.86	4.74	4.41	4.39	0.037	0.063(3)	0.1107	5.8	0.10652	2.8	2.34	3.0	2.56
10_29B	H	2	2.06	1.41	3.75	4.65	1.83	0.099	0.233(3)	0.1153	-0.7	0.10002	4.0	1.66	4.1	1.95
10_30	H	2	2.18	1.32	3.96	3.69	4.42	0.034	0.076(3)	0.1099	4.2	0.10495	3.0	2.45	3.2	2.66
10_31	H	2	1.30	1.10	5.29	5.32	6.36	0.028	0.103(5)	0.1024	-4.9	0.09570	4.8	3.54	4.7	3.64
10_31 II*	H	2	1.06	1.27	6.80	5.22	4.46	0.023	0.107(1)	0.1057	-1.9	0.09875	4.2	3.21	4.2	3.09
Reference material																
MUH-1			4.29	3.41	7.28	18.6	20.4	0.055	0.062(2)	0.1267						
MUH-1 Jaw breaker			5.01	5.22	8.51	9.99	17.0	0.086	0.083(1)	0.1275						
			14.1	78.5	19.2	18.8	13.7	30.3	12.75	0.1142						

CI Chondrite values for $^{187}Os/^{188}Os = 0.1262$ and $^{187}Re/^{188}Os = 0.3915$ (Shirey and Walker (1998) and primitive mantle values for $^{187}Os/^{188}Os = 0.1296$ and $^{187}Re/^{188}Os = 0.434$ (Meisel et al., 2001) (*50*) were used for the calculation of T_{Ma} and T_{RD} ages

* duplicate crushed per hand, without jaw breaker

* *2σ: precision of $^{187}Os/^{188}Os$, including blank contribution

Typical uncertainties on HSE concentrations are 1-4 % RSD, including blank contribution. For some HSE data, the uncertainties are larger due to blank correction and are listed in brackets as for the last significant number

H, harzburgite; D, dunite

Table DR3: Measurements of the UMD Os Standard Solution

SEM	183/188 fc	185/188 fc	186/188 fc	187/188 fc	189/188 fc	190/188 fc	192/188
100 ppb Os STD SEM 1µl 1	0.00014	0.00003	0.1206	0.1140	1.2210	1.9870	3.0872
100 ppb Os STD SEM 1µl 2	0.00012	0.00002	0.1201	0.1141	1.2200	1.9852	3.0905
100 ppb Os STD SEM 1µl 3	0.00006	0.00001	0.1205	0.1141	1.2199	1.9847	3.0832
100 ppb Os STD SEM 1µl 4	0.00010	0.00000	0.1204	0.1142	1.2215	1.9853	3.0946
100 ppb Os STD SEM 1µl 5	0.00014	0.00003	0.1208	0.1141	1.2199	1.9857	3.0900
100 ppb Os STD SEM 1µl 6	0.00245	0.00005	0.1249	0.1139	1.2181	1.9818	3.0703
100 ppb Os STD SEM 1µl 7	0.00015	0.00005	0.1209	0.1141	1.2192	1.9836	3.1052
100 ppb Os STD SEM 1µl 8	0.00018	0.00005	0.1205	0.1141	1.2194	1.9836	3.0908
100 ppb Os STD SEM 1µl 9	0.00051	0.00007	0.1204	0.1140	1.2203	1.9872	3.0940
100 ppb Os STD SEM 1µl 10	0.00008	0.00001	0.1206	0.1141	1.2171	1.9763	3.0635
100 ppb Os STD SEM 1µl 11	0.00012	0.00004	0.1207	0.1140	1.2186	1.9831	3.0835
100 ppb Os STD SEM 1µl 12	0.00008	0.00002	0.1204	0.1142	1.2193	1.9826	3.0871
100 ppb Os STD SEM 1µl 13	0.00013	0.00002	0.1203	0.1142	1.2195	1.9832	3.0882
100 ppb Os STD SEM 1µl 14	0.00003	0.00001	0.1203	0.1141	1.2205	1.9850	3.0854
Mean	**0.0003**	**0.0000**	**0.1208**	**0.1141**	**1.2196**	**1.9839**	**3.0867**
2 x StdDev	0.0013	0.0000	0.0024	0.0002	0.0023	0.0054	0.0203
run no.	14	14	14	14	14	14	14
				2015 (n=8)			
			Mean	**0.1141**			
			2 x StdDev	**0.0002**			
Farraday cups							
35 ppm Os STD SEM 0.5µl			0.1192	0.1138	1.2192	1.9822	3.0778
2 x StdDev			0.0000	0.0000	0.0000	0.0001	0.0001
Shirey & Walker (1998) (*35*)			0.1198	0.1138	1.2197	1.9845	3.0827

Table DR4: Measurements of the UMD Os Standard Solution, "metal free" samples

SEM	183/188 fc	185/188 fc	186/188 fc	187/188 fc	189/188 fc	190/188 fc	192/188
100 ppb Os STD SEM 2µl 1	0.00000	0.00005	0.12001	0.11377	1.21966	1.98303	3.07853
100 ppb Os STD SEM 2µl 2	0.00000	0.00005	0.12005	0.11380	1.22037	1.98769	3.09191
100 ppb Os STD SEM 1µl 1	0.00113	0.00018	0.12155	0.11370	1.22209	1.99231	3.10731
100 ppb Os STD SEM 1µl 2	0.00107	0.00017	0.12189	0.11394	1.21753	1.98793	3.08151
100 ppb Os STD SEM 1µl 3	0.00132	0.00007	0.12143	0.11388	1.22041	1.98789	3.09083
100 ppb Os STD SEM 1µl 4	0.00000	0.00036	0.12244	0.11400	1.22065	1.99252	3.09327
100 ppb Os STD SEM 1µl 5	0.00000	0.00027	0.12394	0.11396	1.22002	1.98295	3.07088
100 ppb Os STD SEM 1µl 6	0.00000	0.00003	0.11994	0.11388	1.22105	1.98862	3.09314
100 ppb Os STD SEM 1µl 7	0.00075	0.00005	0.12048	0.11403	1.21900	1.98941	3.07569
100 ppb Os STD SEM 1µl 8	0.00107	0.00017	0.12189	0.11394	1.21753	1.98793	3.08151
Mean	**0.00053**	**0.00014**	**0.12136**	**0.11389**	**1.21983**	**1.98803**	**3.08646**
2 x StdDev	0.00116	0.00023	0.00256	0.00022	0.00293	0.00639	0.02155
run no.	10	10	10	10	10	10	10

	2017 (n=8)
Mean	**0.1139**
2 x StdDev	**0.0002**